PNAS RESEARCH ARTICLE | BIOCHEMISTRY

Structures of methane and ammonia monooxygenases in native membranes

Frank J. Tucci[a] and Amy C. Rosenzweig[a,1]

Edited by Janet Smith, University of Michigan-Ann Arbor, Ann Arbor, MI; received September 3, 2024; accepted November 22, 2024

Methane- and ammonia-oxidizing bacteria play key roles in the global carbon and nitrogen cycles, respectively. These bacteria use homologous copper membrane monooxygenases to accomplish the defining chemical transformations of their metabolisms: the oxidations of methane to methanol by particulate methane monooxygenase (pMMO) and ammonia to hydroxylamine by ammonia monooxygenase (AMO), enzymes of prime interest for applications in mitigating climate change. However, investigations of these enzymes have been hindered by the need for disruptive detergent solubilization prior to structure determination, confounding studies of pMMO and precluding studies of AMO. Here, we overcome these challenges by using cryoEM to visualize pMMO and AMO directly in their native membrane arrays at 2.4 to 2.8 Å resolution. These structures reveal details of the copper centers, numerous bound lipids, and previously unobserved components, including identifiable and distinct supernumerary helices interacting with pMMO and AMO, suggesting a widespread role for these helices in copper membrane monooxygenases. Comparisons between these structures, their metallocofactors, and their unexpected protein–protein interactions highlight features that may govern activity or the formation of higher-order arrays in native membranes. The ability to obtain molecular insights within the native membrane will enable further understanding of these environmentally important enzymes.

membrane protein | metalloenzyme | cryoEM | methane oxidation | ammonia oxidation

Significance

Methane- and ammonia-oxidizing bacteria regulate the atmospheric levels of the potent greenhouse gases methane and nitrous oxide. These bacteria use the enzymes particulate methane monooxygenase (pMMO) and ammonia monooxygenase (AMO) to oxidize methane and ammonia, respectively, difficult reactions of biotechnological interest. Destabilization of these enzymes upon isolation from the bacterial membranes has complicated investigations of pMMO and precluded structural studies of AMO. We circumvented this challenge by visualizing pMMO and AMO directly in their native membranes to high resolution using cryoEM. This work provides the most biologically relevant view of pMMO to date and the structure of AMO, setting the stage for detailed structural investigation of these and other challenging membrane proteins.

Limiting global warming to 1.5 to 2 °C by the end of the century requires not only decreasing carbon dioxide emissions, but also diminishing contributions from methane and nitrous oxide, the second- and third-most impactful greenhouse gases, respectively (1, 2). Aerobic microbial processes are important sources and sinks for these gases, with methane-oxidizing bacteria (methanotrophs) consuming methane and ammonia-oxidizing bacteria (nitrifiers) releasing nitrous oxide (3–5). Methanotrophs and nitrifiers use copper-dependent membrane monooxygenases (6) to carry out the first and most chemically difficult transformations in their metabolisms: the conversions of methane to methanol by particulate methane monooxygenase (pMMO) and ammonia to hydroxylamine by ammonia monooxygenase (AMO) (5, 7). Due to the loss of enzymatic activity upon removal from their native intracytoplasmic membranes (ICMs), understanding the structures and mechanisms of pMMO and AMO has posed significant challenges.

Initial crystal structures of pMMO revealed the $\alpha_3\beta_3\gamma_3$ trimeric arrangement of its three subunits, PmoB, PmoA, and PmoC, as well as the presence of three copper sites: the bis-His and the Cu_B sites in PmoB, and the Cu_C site in PmoC, each of which was ultimately shown to bind one copper ion (8–14). The crystal structures, derived from inactive purified pMMO solubilized in detergent, lacked a highly conserved ~30 residue region of the transmembrane PmoC subunit (15). This region was finally resolved by cryoelectron microscopy (cryoEM) single particle analysis (SPA) of pMMO reconstituted into nanodiscs prepared with native methanotroph lipids, which also enabled a partial recovery of activity (16). These cryoEM structures of active pMMO unveiled a fourth copper center, denoted Cu_D and located approximately 5.7 Å away from Cu_C. Simultaneous occupancy of Cu_C and Cu_D has not been observed, but subsequent studies using parallel electron paramagnetic resonance (EPR) spectroscopy and cryoEM unambiguously identified Cu_D as a Cu(II) ion and associated its loading with pMMO activity (17). Furthermore, combined electron double nuclear resonance (ENDOR) spectroscopic and cryoEM data showed that the active site probe and product inhibitor 1,1,1-trifluoroethanol binds in the pocket housing the Cu_C and Cu_D sites, identifying it as the active site of pMMO (17). Despite its sequence similarity to pMMO, ability to oxidize methane (18, 19), and apparent dependence on copper for activity (20, 21), attempts to study AMO using similar approaches have been unsuccessful thus far, a challenge further compounded by the slow growth rate of nitrifiers.

Author affiliations: [a]Departments of Molecular Biosciences and of Chemistry, Northwestern University, Evanston, IL 60208

Author contributions: F.J.T. and A.C.R. designed research; F.J.T. performed research; F.J.T. and A.C.R. analyzed data; and F.J.T. and A.C.R. wrote the paper.

The authors declare no competing interest.

This article is a PNAS Direct Submission.

[1]To whom correspondence may be addressed. Email: amyr@northwestern.edu.

This article contains supporting information online at https://www.pnas.org/lookup/suppl/doi:10.1073/pnas.2417993121/-/DCSupplemental.

Published December 31, 2024.

Thus, details of the AMO molecular architecture and copper active site remain unknown.

The characterization of pMMO in native lipid nanodiscs provided critical insight into the active site, but questions remain regarding the biological relevance of these studies. The methane oxidation activity recovered in nanodiscs is less than that of pMMO in native membranes, which in turn is less than that in whole cells (5). As with many complex membrane protein systems (22), purification of pMMO from the membrane may distort its structure or remove cofactors important for function. Indeed, pMMO forms densely packed hexagonal arrays in the ICMs, recently observed in cryo-focused ion beam (cryoFIB) milled lamellae of *Methylococcus capsulatus* (Bath) cells (23). While an ideal study of pMMO would involve visualization directly in whole cells at high resolution, recent cryoelectron tomography (cryoET) subtomogram averaging (STA) of *M. capsulatus* (Bath) lamellae only yielded a low-resolution (15 Å) map. The resolution was improved to 4.8 Å by using isolated ICMs, which preserve the pMMO arrays, but side chains, copper sites, endogenous molecules such as lipids, and interactions between neighboring pMMO trimers in the arrays were not resolved (23). Here, we have instead used cryoEM SPA to determine structures of pMMOs from *M. capsulatus* (Bath) and *Methylocystis* species (sp.) Rockwell and of AMO from *Nitrosomonas europaea* directly in native membranes at high resolution (2.4 to 2.8 Å).

Results

Structures of pMMO in Native Membranes. We began structure determination by isolating highly active, pMMO-containing membranes from *M. capsulatus* (Bath) cells (*SI Appendix*, Fig. S1). The membranes were applied to cryoEM grids for data collection and SPA. As observed previously (16, 23, 24), the pMMO trimers in isolated membranes are organized in hexagonal arrays (Fig. 1*A* and *SI Appendix*, Figs. S2 and S3), consistent with those observed in whole cells (23). As described in the Materials and Methods, pMMO particles were picked, classified, and aligned in an iterative manner to yield 2.4 to 2.6 Å resolution 3D reconstructions of pMMO in the native membrane arrays (Fig. 1 *B–F* and *SI Appendix*, Figs. S2–S5 and Table S1). In contrast to the cryoET map (23), the single particle cryoEM map reveals well-defined side chains, copper centers, lipids, and previously unobserved densities interacting with the pMMO subunits (Fig. 1 *B–F* and *SI Appendix*, Figs. S4 and S5). While the adjacent trimers in the array are clearly visible (Fig. 1*B*), high resolution could not

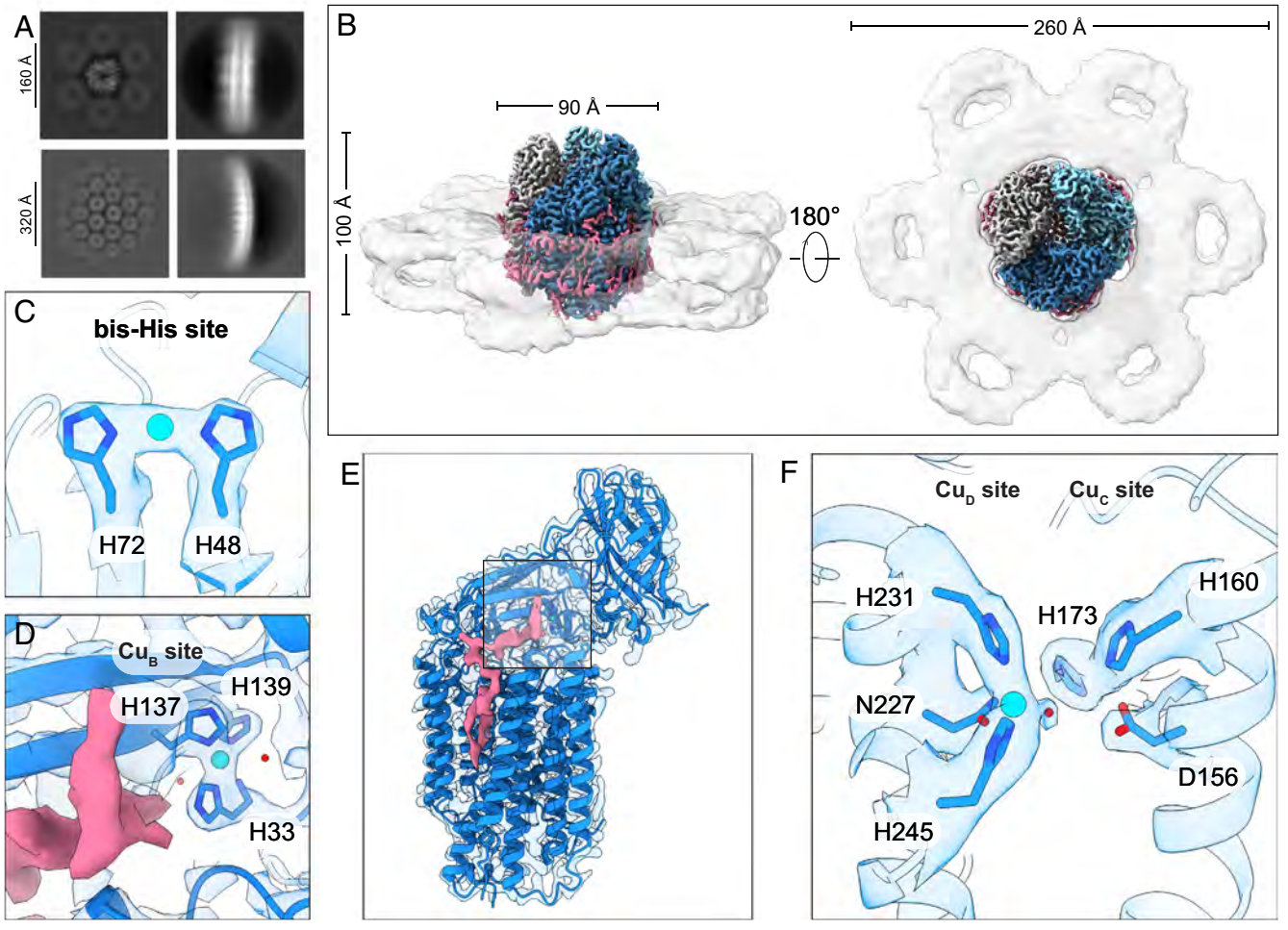

Fig. 1. Single particle cryoEM of *M. capsulatus* (Bath) pMMO in native membranes. (*A*) Representative 2D class averages of pMMO in native membranes showing the hexagonal arrays of pMMO trimers. Top–down (*Left*) and side-on (*Right*) views are shown with box sizes of 400 (*Top*) and 800 (*Bottom*) pixels. The 2D class averages at a box size of 400 pixels show secondary structure features including alpha helices. (*B*) 3D reconstruction of pMMO in the unwashed native membrane array at 2.6 Å global resolution showing the C3 symmetrical protomers of pMMO in blue, light blue, and gray. Lipid densities and densities not corresponding to the pMMO subunits are colored pink, and the low-resolution densities corresponding to the surrounding pMMOs in the hexagonal array are shown in transparent gray. (*C*) bis-His site with copper ion shown in cyan and cryoEM density superimposed (transparent blue, 8σ). (*D*) Cu_B site with proximal unidentified density in pink, copper ion shown in cyan, and cryoEM density superimposed (8σ). Water molecules are shown as red spheres. (*E*), Model of one protomer with cryoEM map superimposed in transparent blue with unidentified membrane-associated density in pink (8σ). (*F*) Cu_C and Cu_D sites with cryoEM density superimposed (4.5σ) showing a copper ion occupying Cu_D and an empty Cu_C site. The cryoEM maps in (*C–F*) are of the washed membranes at 2.4 Å resolution.

be obtained upon processing with either C1 or C3 symmetry. It may be that the neighboring pMMOs do not form stable protein–protein interactions, or that these interactions lack clear symmetrical arrangements in the context of hexagonal arrays.

Having established the feasibility of high-resolution SPA of pMMO in native membranes, we compared the effects of different sample preparation methods, including reconstitution into native lipid nanodiscs (16) and detergent solubilization, on the cryoEM maps (Fig. 2 *A*–*D* and *SI Appendix*, Figs. S5–S9). pMMO-containing membranes are typically isolated by cell sonication, low-speed centrifugation to remove cellular debris, and three rounds of ultracentrifugation and Dounce homogenization in fresh buffer. The resulting "washed" membranes yielded the highest resolution (2.4 Å) structure (Figs. 1 *C*–*F* and 2*B* and *SI Appendix*, Figs. S5*C* and S6). While these steps eliminate contaminants and concentrate pMMO-containing membranes, we hypothesized that extensive washing might remove essential membrane components or disrupt the pMMO arrays. We therefore tested two alternative workflows. First, *M. capsulatus* (Bath) cells were lysed, followed by gentle centrifugation and direct SPA on pMMO in the clarified lysate ("unwashed" membranes). Remarkably, simply breaking open the cells yielded a 2.6 Å resolution cryoEM structure (Figs. 1*B* and 2*C* and *SI Appendix*, Figs. S5*D* and S7). The lipid densities are stronger than those observed in the cryoEM maps of pMMO in washed membranes. In addition, clear low-resolution densities for neighboring pMMOs in the hexagonal arrays surround a central pMMO visualized at high resolution (Fig. 1*B*). In the second workflow, we performed in vivo crosslinking of *M. capsulatus* (Bath) cells using paraformaldehyde (25), followed by membrane isolation with a single wash cycle of ultracentrifugation and homogenization. The resultant 2.6 Å resolution cryoEM map showed the strongest density for the membrane bilayer (Fig. 2*D* and *SI Appendix*, Figs. S5*E* and S8). In all cases, the lipid densities are more numerous and well-defined than those in maps of pMMO in native lipid nanodiscs (Fig. 2*A* and *SI Appendix*, Fig. S5*B*).

We were able to model these densities with 57 phosphatidylethanolamine (PE) lipids interacting with the pMMO trimer, showing good agreement with the cryoEM map (Fig. 2*E*). We selected PE(16:0_17:1) as the model lipid as it is the most abundant in our prior lipidomics analysis of *M. capsulatus* (Bath) cells (16). PE lipids overall were most highly represented, comprising 46% of the total lipids. Lipids with one degree of unsaturation comprised 61% of the total composition and lipids with a 16-carbon acyl tail comprised 55% of the total (*SI Appendix*, Fig. S10*A*). PE(16:0_17:1) satisfies each of these requirements, and is therefore a suitable proxy for modeling membrane phospholipids in these cryoEM maps. These lipids engage in numerous hydrogen bonding or salt bridge interactions between their head groups and lysine and arginine residues that flank the transmembrane region of pMMO (*SI Appendix*, Fig. S10 *B*–*F*).

We then extended the workflow for studying pMMO in native membranes from *M. capsulatus* (Bath), a type X (a subset of type I) gammaproteobacterial methanotroph, to pMMO from another species, *M.* sp. Rockwell, a type II alphaproteobacterial methanotroph. Type II methanotrophs have a different ICM morphology than type I methanotrophs (26), raising the question of whether their ICMs contain hexagonal pMMO arrays like those in *M. capsulatus* (Bath). The 2D class averages of pMMO-containing *M.* sp. Rockwell membranes clearly show hexagonal array patterning, and yielded a 2.5 Å resolution structure of *M.* sp. Rockwell pMMO (Fig. 3 *A*–*C* and *SI Appendix*, Fig. S11). As in the crystal structure (10) and cryoEM structure in lipid nanodiscs (16), additional density corresponding to a transmembrane helix adjacent to PmoC and extending from the periplasm to the cytoplasm is observed (Fig. 3 *B*–*D*). Prior efforts to identify this helix via mass spectrometry or inspection of side chain densities were not successful (10), but this cryoEM map allowed for automatic building with ModelAngelo (27), yielding a 23 residue sequence that corresponds to a 23 residue protein of unknown function encoded in the *M.* sp. Rockwell genome (*SI Appendix*, Table S2). As such, it represents a previously unknown supernumerary subunit associated with a pMMO. Notably, extra density between protomers in the *M. capsulatus* (Bath) maps, though of insufficient quality for reliable visual sequencing, can be modeled with a small transmembrane helix, suggesting a widespread role for supernumerary helices in pMMOs (*SI Appendix*, Fig. S12).

pMMO Copper Centers in Native Membranes. An important motivation for studying pMMO in native membranes is to determine the structures and occupancies of the copper centers in samples that have not been subjected to extensive biochemical manipulation. A number of questions remain unresolved regarding each of the copper centers. First, the biological relevance of the bis-His site is unclear. One of its two histidine ligands, His48, is not highly conserved, and the site is only occupied in the *M. capsulatus* (Bath) pMMO structures (5). Thus, the bis-His site could derive from adventitious copper binding during pMMO isolation, purification, reconstitution into nanodiscs, and/or crystallization. However, there is strong density corresponding to a copper ion in the bis-His site in all the structures of *M. capsulatus* (Bath) pMMO in native membranes (Fig. 1*C*), indicating that the site is not an artifact.

Once thought to be the active site, Cu_B is coordinated by three histidine residues, along with the amino group of the PmoB N-terminal histidine. These three histidines are not conserved in a subset of pMMOs from Verrucomicrobia, an observation that, along with its presence as Cu(II) and saturated coordination, indicates that Cu_B is not the pMMO active site. Nonetheless, replacement of one Cu_B histidine ligand in a related hydrocarbon monooxygenase decreased activity significantly (28), suggesting a functional role for this site. Consistent with all the prior structural and spectroscopic studies, the structures of pMMO from both *M. capsulatus* (Bath) and *M.* sp. Rockwell in native membranes show that Cu_B is a monocopper site in the native membranes, with all three histidine side chain nitrogens and the amino group of His33 (*M. capsulatus* Bath numbering) as ligands (Figs. 1*D* and 3*E*). Axial water ligands are also present, as shown by ENDOR spectroscopic analysis (12, 14) and prior crystal and cryoEM structures (5, 10, 16, 17).

Notably, the cryoEM map of *M. capsulatus* (Bath) pMMO in native membranes reveals an unidentified density extending from the membrane into the Cu_B site (Fig. 1 *D* and *E* and *SI Appendix*, Fig. S13). The periplasmic part of this density appears to engage in a parallel β-sheet interaction with the edge β-strand of the N-terminal PmoB cupredoxin-like domain, and connects to the head group of a multitailed lipid, perhaps a cardiolipin, density interacting with the PmoC transmembrane region (Fig. 1*E* and *SI Appendix*, Fig. S13). This density has not been observed in any prior pMMO structures, including the low-resolution cryoET STA structure of membrane-bound pMMO (*SI Appendix*, Fig. S4).

The PmoC active site region housing the Cu_C and Cu_D sites is susceptible to distortions upon removal from the native membranes, as evidenced by its disorder in crystal structures (5, 15). To differentiate the effects of crystallization from those of detergent solubilization, we determined the 2.9 Å resolution cryoEM structure of pMMO solubilized in 0.02% n-dodecyl-β-D-maltoside (DDM) (*SI Appendix*, Fig. S9 and Table S1) as such samples have been used extensively for spectroscopy and are the starting point

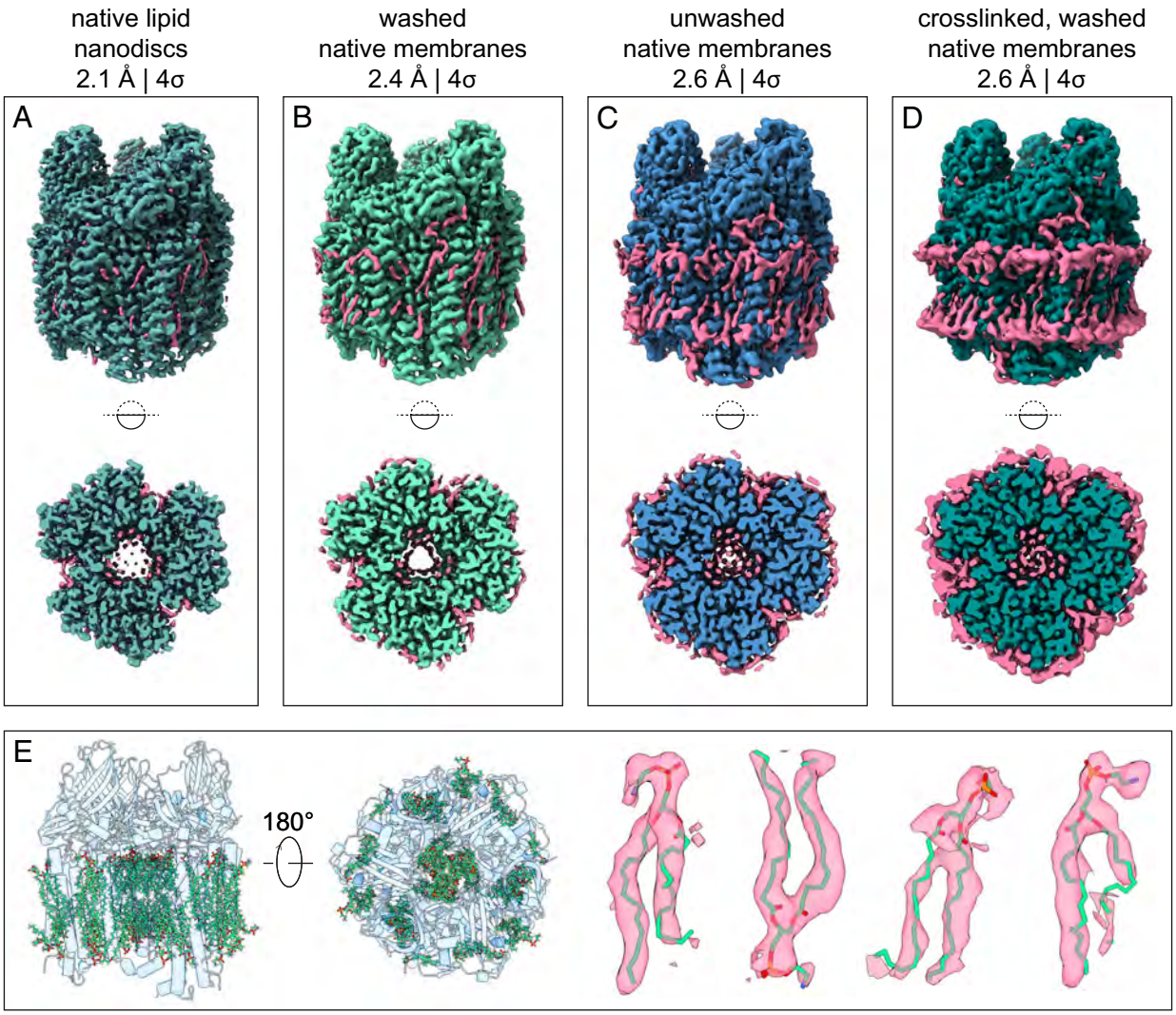

Fig. 2. Effects of biochemical manipulation on pMMO cryoEM maps. (*A*) pMMO in native lipid nanodiscs showing associated lipid densities (pink). (*B–D*) pMMO in washed membranes, unwashed membranes, and crosslinked, washed membranes showing strong lipid densities and unidentified membrane components (pink). (*E*) Model of pMMO in unwashed membranes with helices shown as cylinders and modeled lipids as sticks. Representative lipids [modeled as PE(16:0_17:1)] are shown with the corresponding cryoEM density superimposed (pink, 3σ).

for nanodisc reconstitution (13, 16). In contrast to the previously reported 0.05% DDM pMMO cryoEM structure by Chan et al. (29), density for all of PmoC is present, with weaker density for the Cu_D ligands and occupancy of the Cu_C site (*SI Appendix*, Fig. S14). Thus, detergent affects the differential occupancy of the two sites. While Chan et al. reported additional copper ions in the PmoB and PmoA subunits in the 0.05% DDM structure (29), the 0.02% DDM structure contains only mononuclear bis-His and Cu_B sites (*SI Appendix*, Fig. S15).

Given the effects of detergent on the PmoC active site region, the Cu_C and Cu_D sites might be expected to differ in native membranes that have never been in contact with detergent. However, the structures of *M. capsulatus* (Bath) pMMO in native membranes show an empty Cu_C site and an occupied Cu_D site, as observed in the native lipid nanodisc structures (16, 17) (Fig. 1*F*). Importantly, this result establishes that the unoccupied Cu_C site in the nanodisc samples is not responsible for the decreased methane oxidation activity of native lipid nanodiscs compared to pMMO-containing membranes. Instead, the membrane bilayer itself, the hexagonal pMMO arrays, and/or some cofactor(s) present in the membranes must contribute to optimal pMMO activity. The biological relevance of Cu_D is further supported by the structure of *M.* sp. Rockwell pMMO in native membranes, which shows occupancy of the Cu_D site, but not the Cu_C site (Fig. 3*F*), agreeing with the structures of *M. capsulatus* (Bath) pMMO in nanodiscs (16) and in native membranes (Fig. 1*F*). By contrast, the cryoEM map of *M.* sp. Rockwell pMMO in synthetic lipid nanodiscs showed density for a copper ion occupying the Cu_C but not the Cu_D site (16).

Structure of AMO in Native Membranes. The ammonia oxidizer *N. europaea* produces ICMs (3, 30) similar to those in many methanotrophs, and cryoEM of isolated membranes revealed hexagonal arrays of particles (Fig. 4*A* and *SI Appendix*, Fig. S16) resembling the pMMO arrays in *M. capsulatus* (Bath) and *M.* sp. Rockwell membranes. With minimal sample (~0.5 g cell mass), we were able to obtain a 2.8 Å cryoEM structure of AMO in its native membranes (Fig. 4 *B* and *C* and *SI Appendix*, Fig. S16). Like pMMO, AMO comprises an $\alpha_3\beta_3\gamma 3$ trimeric architecture of the AmoB, AmoA, and AmoC subunits. The AMO structure also reveals an unexpected transmembrane helix closely associated with the AmoC subunit in an interaction mediated by a transmembrane phospholipid (Fig. 4 *B–D*). This helix is much longer than that in *M.* sp. Rockwell pMMO (Fig. 3

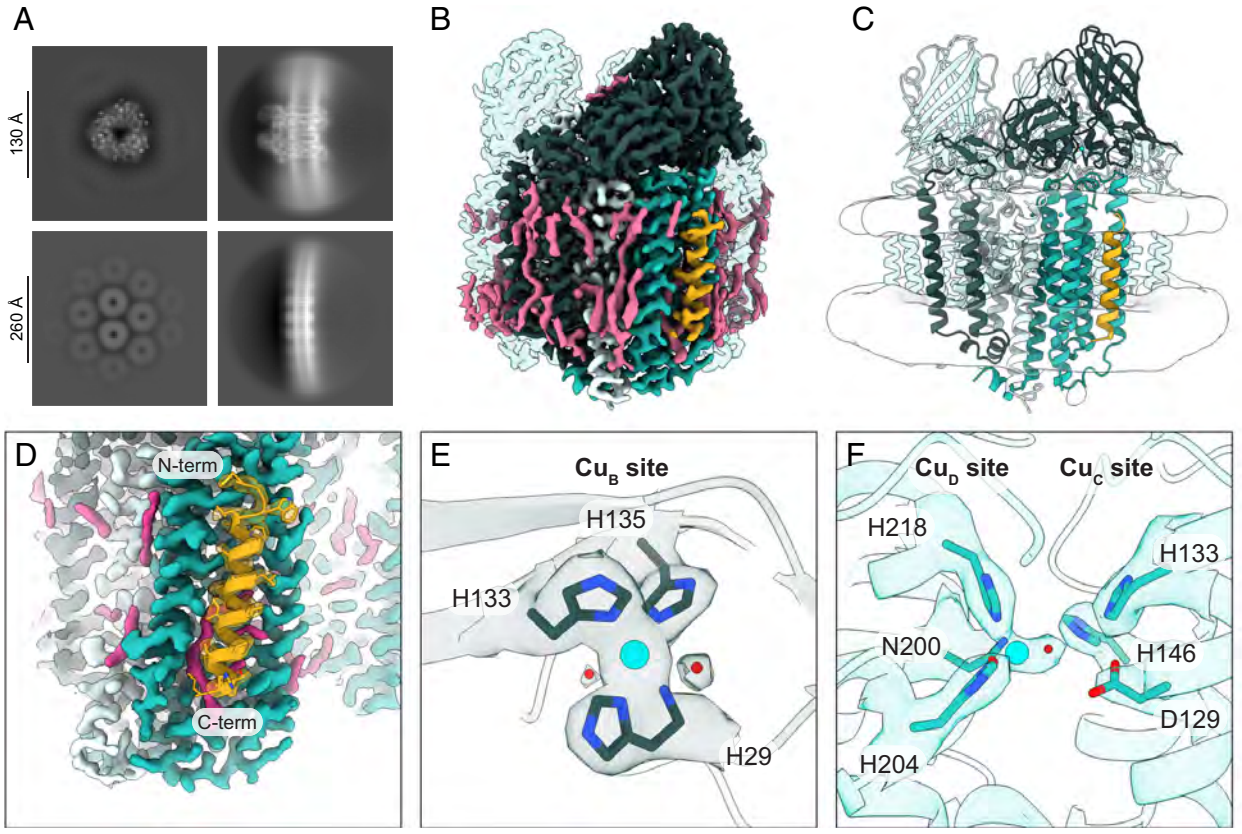

Fig. 3. Structure of pMMO from *M.* sp. Rockwell in its native membrane. (*A*) 2D class averages of pMMO in native membranes showing secondary structure features and hexagonal pMMO arrays in native membranes, shown from top–down (*Left*) and side-on (*Right*) views with box sizes of 320 (*Top*) and 640 (*Bottom*) pixels. (*B*) CryoEM map of pMMO from *M.* sp. Rockwell at 2.5 Å resolution with one protomer highlighted, including PmoB (dark green), PmoA (light green), PmoC (teal), the extra helix (gold), and membrane-associated densities (pink). (*C*) CryoEM model of *M.* sp. Rockwell pMMO with one protomer highlighted, including PmoB (dark green), PmoA (light green), PmoC (teal), and the extra helix (gold). The transparent gray density corresponds to the membrane bilayer. (*D*) CryoEM map in teal with density overlaid on the helix model (gold) and membrane-associated densities shown in pink (4σ). (*E*) Cu_B site shown with cryoEM map superimposed (8σ). Water molecules are shown as red spheres. (*F*) Cu_C and Cu_D sites with cryoEM density superimposed (5σ) showing an occupied Cu_D and empty Cu_C site, along with a water molecule coordinated to Cu_D.

B–D) and adopts the opposite orientation, with its N terminus on the cytoplasmic side and its C-terminus on the periplasmic side of the membrane (*SI Appendix*, Fig. S17). The sequence obtained with ModelAngelo (27) corresponds to an unannotated 46 residue open reading frame in the *N. europaea* genome, of which 39 residues were readily modeled in the cryoEM map (Fig. 4*D* and *SI Appendix*, Table S2). Adjacent to this helix is a periplasmic stretch of density that is well modeled as a 14-residue peptide, but its identity and whether it is associated with the helix remain unclear (*SI Appendix*, Fig. S18).

The residues coordinating the pMMO Cu_B, Cu_C, and Cu_D sites are conserved in *N. europaea* AMO, and these sites are present in the AMO structure. Similar to pMMO, Cu_B is ligated by three histidine residues, including the N-terminal histidine, as well as two axial water molecules (Fig. 4*E*). In contrast with the structures of pMMOs in native membranes, the Cu_C site is occupied while the neighboring Cu_D site is empty (Fig. 4*F*). Although the density for the AmoC subunit is sufficient for model building, the density in the region that houses the Cu_D site is diminished as compared to the rest of the AmoC subunit. These observations are consistent with pMMO structures showing that Cu_C is occupied when the ligands to the Cu_D site are disordered. It is striking that the density for this region is weak despite the omission of biochemical manipulations and detergent solubilization in the preparation of AMO membranes. This relative fragility of AMO outside of the cellular environment may explain the absence of activity in isolated preparations and the lack of success in prior efforts to determine the structure.

Discussion

These structures of pMMO and AMO in native membranes provide views of these enzymes at high resolution in biologically relevant environments. The results demonstrate how biochemical manipulations disrupt the native membrane components associated with the enzymes in vivo, likely contributing to the loss of enzymatic activity upon purification (3, 5, 16, 31). The structures of pMMOs from *M. capsulatus* (Bath) and *M.* sp. Rockwell in native membranes show the Cu_D site at high resolution, identifying this site in a species other than *M. capsulatus* (Bath) and supporting its importance in methane oxidation. The structure of *N. europaea* AMO in native membranes reveals its molecular architecture and copper sites, along with a supernumerary transmembrane helix that associates with AmoC. The identification of the *M.* sp. Rockwell pMMO and *N. europaea* AMO supernumerary helices provides candidates for functional partners. Although these helices differ in size and orientation, they interact with pMMO and AMO at similar locations, and could mediate array formation or other aspects of activity within the ICM ultrastructure. Observation of a similar supernumerary helix in *M. capsulatus* (Bath) pMMO supports the widespread importance of these helices in copper membrane monooxygenases. Additional yet-to-be-identified densities interacting with the PmoB Cu_B site and the AmoB subunit warrant further investigation as well. Comparisons between these structures of pMMO and AMO in native membranes underscore the potential importance of these features for biological methane

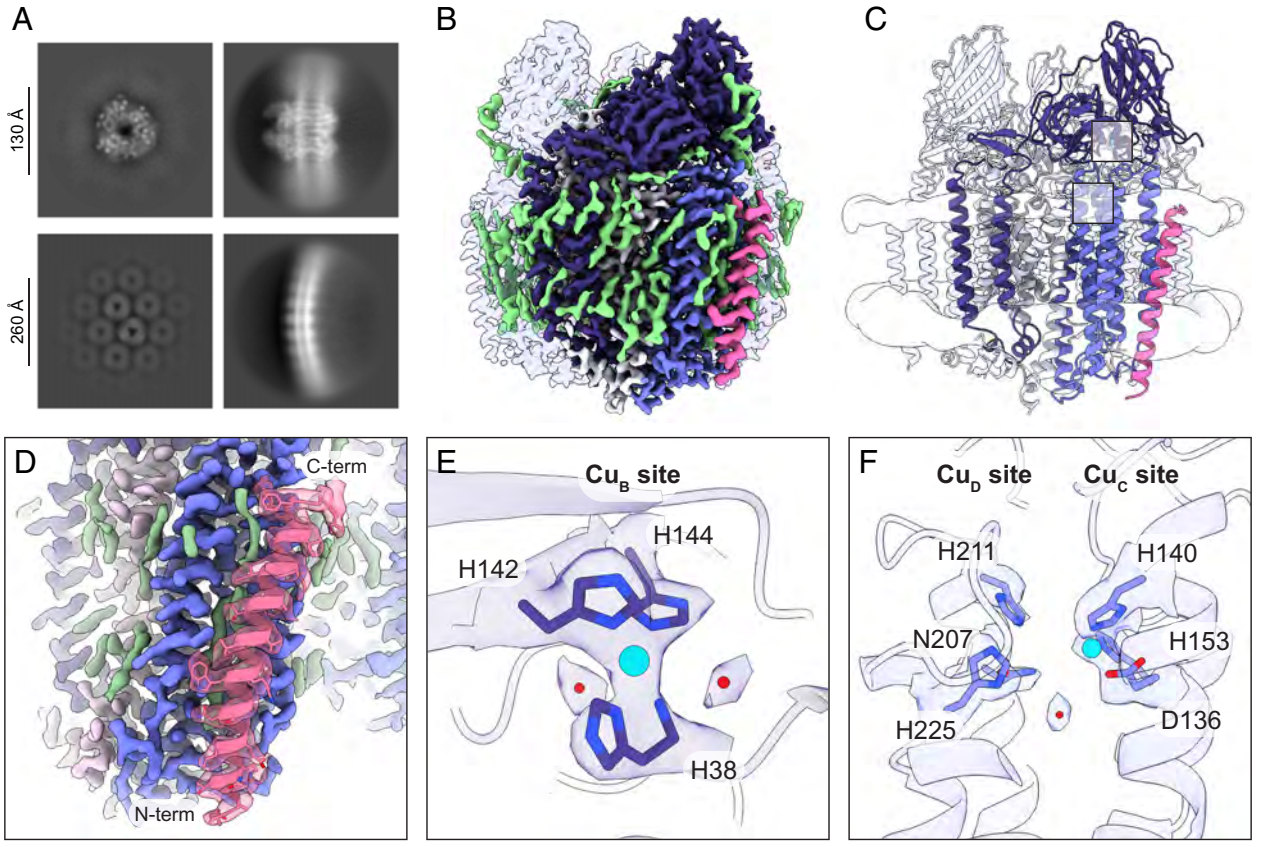

Fig. 4. Structure of AMO in native membranes from *N. europaea*. (*A*) 2D class averages of AMO in native membranes from *N. europaea* showing secondary structure features, the native membrane, and hexagonal AMO arrays in native membranes, shown from top–down (*Left*) and side-on (*Right*) views at box sizes of 320 (*Top*) and 640 (*Bottom*) pixels. (*B*) 2.8 Å resolution cryoEM map of AMO with one protomer highlighted showing AmoB (dark purple), AmoA (light purple), AmoC (purple), the extra helix (pink), and membrane-associated densities (green). (*C*) CryoEM model of AMO highlighting one protomer of AmoB (dark purple), AmoA (light purple), AmoC (purple), and the extra helix (pink), along with transparent density indicating the native membrane bilayer and squares indicating the copper sites. (*D*) CryoEM map with transparent density overlaid for the extra helix (pink, 5σ) and membrane-associated lipid densities (green, 4σ). (*E*) Cu_B site coordinated by histidines with transparent cryoEM density superimposed (8σ). Water molecules are shown as red spheres. (*F*) Cu_C and Cu_D sites with cryoEM map superimposed (5σ) showing an occupied Cu_C and empty Cu_D site.

and ammonia oxidation. Our cryoEM SPA of native membranes, which enables high-resolution structure determination from minimal biomass while circumventing the need for detergent solubilization and protein purification, provides a roadmap for future studies of pMMO and AMO. Moreover, visualization of the AMO structure after years of efforts highlights the power of this approach and its potential generalizability to other difficult membrane protein targets.

Materials and Methods

Growth of Methanotrophic Bacteria. *M. capsulatus* (Bath) was cultivated at 45 °C in a 12 L fermentor (BioFlo 4500, New Brunswick Scientific). The liquid growth medium was composed of 1× nitrate mineral salts, 3.9 μM phosphate buffer (adjusted to pH 6.8), 40 μM NaFe(III)EDTA, trace elements, and 50 μM $CuSO_4$. Cells were agitated at 200 rpm with a 1:3 methane:air ratio at a flow of 1 L/min. Upon reaching an optical density at 600 nm (OD_{600}) of 8 to 10, cells were harvested by centrifugation at 5,000×*g* for 25 min, frozen in liquid nitrogen, and stored at −80° C.

Isolation of pMMO-Containing Membranes. *M. capsulatus* (Bath) cells were suspended in buffer containing 25 mM PIPES (pH 7.3) and 250 mM NaCl supplemented with DNase (Sigma-Aldrich) and EDTA-free complete protease inhibitor cocktail (Sigma-Aldrich). Following resuspension, the cells were disrupted by sonication at 80% power (45 amplitude, 1 s on and 1 s off) for 10 min using a QSonica Q700 instrument. The resulting lysate was clarified by centrifugation first at 10,000×*g* for 45 min. At this point, unwashed membrane samples were applied to cryoEM grids for vitrification and data collection. For washed membrane samples, the clarified lysate was centrifuged again at 10,000×*g* for 25 min. Subsequently, membranes were isolated by ultracentrifuging the supernatant at 150,000×*g* for 1 h. The pelleted membranes were washed in a 40 mL Dounce homogenizer with fresh PIPES buffer, followed by ultracentrifugation at 150,000×*g* for 30 min. This washing process was repeated twice followed by resuspension of the washed membrane pellet in a 7 mL Dounce homogenizer.

Crosslinked washed membranes were prepared by in vivo crosslinking whole cells using 4% paraformaldehyde, which were then lysed as described above. The lysate was clarified by centrifugation at 10,000×*g* for 45 min, and then the crosslinked membranes were isolated by ultracentrifugation at 150,000×*g* for 1 h. The pellet containing crosslinked membranes was then resuspended in the lysis buffer using a 7 mL Dounce homogenizer and applied to cryoEM grids for vitrification and data collection. For all samples, the protein concentration was determined by the DC Lowry Assay (Bio-Rad) before application to cryoEM grids for vitrification and data collection.

Detergent Solubilization of pMMO from Native Membranes. pMMO was extracted from the membranes with n-dodecyl-β-D-maltopyranoside (DDM). DDM was added to membranes at a ratio of 1.2 mg DDM per 1 mg pMMO, followed by gentle end-over-end mixing at 15 rpm for 1 h at 4 °C. To eliminate residual membranes and aggregated protein, the solution was clarified by centrifugation for 1 h at 150,000×*g*, and the resulting pellet was discarded. The solubilized pMMO was then transitioned into a buffer solution comprising 25 mM PIPES (pH 7.3), 250 mM NaCl, and 0.02% DDM using Amicon concentrators (MilliporeSigma) with a molecular weight cutoff of 100 kDa. The concentration was determined using the DC Lowry (Bio-Rad) assay with BSA as a standard.

Methane Oxidation Activity Assay. Samples of 100 μL pMMO were diluted to a concentration of 0.5 to 2 mg mL^{-1} and mixed with an excess of duroquinol, or with 4 mg mL^{-1} NADH for native membranes, in 2 mL screw-top vials (Agilent). 1 mL of the headspace gas was removed from the vials and replaced with 1.5 mL of ^{13}C methane (Sigma-Aldrich). For each independent sample, 3 technical replicates were prepared. Control vials without methane and duroquinol were also prepared. The reaction mixture was then shaken at 200 rpm in a water bath at 45 °C for 5 min and subsequently frozen at −20 °C. For GC/MS measurement of ^{13}C methanol product, 500 μL of chloroform containing 1 mM dichloromethane was added to each sample. The vials were shaken at 200 rpm for 10 min, followed by centrifugation at 2,000×*g* for 10 min. A volume of 2.5 μL of each sample was then injected onto a PoraBOND Q column (25 m × 250 μm × 3 μm) in an Agilent 7890B/5977A MSD GC/MS instrument with a split ratio of 10:1. Helium was used as the carrier gas at a constant flow rate of 1.2 mL min^{-1}. The oven temperature program was as follows: starting at 80 °C for 3.5 min, ramping up at 50 °C min^{-1} to 150 °C, and holding for 1.5 min, followed by a second ramp at 15 °C min^{-1} to a final temperature of 300 °C, which was held for 1 min. The mass spectrometer was operated at a source temperature of 230 °C, quadrupole temperature of 150 °C, electron ionization at 70 eV, and a detector voltage of 2,999 V. The ions with m/z values of 31, 33, and 49 were monitored to detect ^{12}C methanol, ^{13}C methanol, and dichloromethane, respectively. The ^{13}C methanol peak was integrated, quantified against a standard curve, and normalized to the concentration of dichloromethane.

Growth of *N. europaea*. *Nitrosomonas europaea* ATCC 19718 was grown in a mineral medium containing per liter: 10 mM $(NH_4)_2SO_4$, 0.4 mM KH_2PO_4, 0.2 mM $MgSO_4{\cdot}7H_2O$, 1.0 mM $CaCl_2{\cdot}2H_2O$, 1.0 mM KCl, 0.02% phenol red, 1 mL Trace solution (which contains per liter Milli-Q water: 11.5 mM Na_2-EDTA, 10.0 mM $FeCl_2{\cdot}4H_2O$, 0.50 mM $MnCl_2{\cdot}2H_2O$, 0.10 mM $NiCl_2{\cdot}6H_2O$, 0.10 mM $CoCl_2{\cdot}6H_2O$, 0.10 mM $CuCl_2{\cdot}2H_2O$, 0.50 mM $ZnCl_2$, 0.10 mM $Na_2MoO_4{\cdot}2H_2O$, and 1.0 mM H_3BO_3), 15 mM HEPES buffer all dissolved in 1,000 mL total Milli-Q water. The pH of the media was adjusted using 1 M or 10 M NaOH to ca. pH 7.6 to 7.8. 100 mL of media was poured aseptically into 250 mL Wheaton bottles with septum caps. Bottles were then inoculated with 1 mL of late log phase culture. Cultures were incubated at 30 °C with shaking (100 rpm). During growth, the pH was maintained at approximately 7.7 using 5% sodium bicarbonate that was added daily after the first 48 h of growth using sterile syringes. Growth was assessed by nitrite accumulation, and cells were harvested at 12 to 15 mM nitrite by filtration. Filters were washed with HEPES buffer, and cells were collected into 15 mL Falcon tubes and stored at −80 °C prior to shipping.

Isolation of AMO-Containing Membranes from *N. europaea*. Approximately 0.5 g of frozen *N. europaea* cells were resuspended at 4 °C in ~100 mL of buffer containing 25 mM PIPES (pH 7.3) and 250 mM NaCl supplemented with DNase (Sigma-Aldrich) and cOmplete EDTA-free protease inhibitor cocktail (Sigma-Aldrich). Resuspended cells were lysed by sonication at 80% power (45 amplitude, 1 s on and 1 s off) for 10 min using a QSonica Q700 instrument. The resulting lysate was first clarified by centrifugation at 10,000×*g* for 45 min, and then AMO-containing membranes were pelleted by ultracentrifugation at 150,000×*g* for 1 h. The resulting pellet was then resuspended in fresh buffer by homogenization using a 7 mL Dounce homogenizer.

CryoEM Sample Preparation and Data Collection. The isolated membrane samples were diluted to approximately 4 to 5 mg mL^{-1} as measured by the DC Lowry (Bio-Rad) assay and applied to C-Flat holey carbon copper grids with 1.2 μm holes, 1.3 μm spacing, and 400 mesh (Electron Microscopy Sciences) with an FEI Vitrobot. Prior to sample application, plasma cleaning of grids was performed using a Solarus plasma cleaner (Gatan) for 10 s at a voltage of 10 W. Within the Vitrobot chamber, 3 μL of the sample were applied to the grids under conditions of 100% humidity and 4 °C. Samples were then blotted using a wait time of 30 s, a blot time of 4 s, and a blot force of 5, followed by vitrification in liquid ethane and storage in liquid nitrogen. CryoEM data were acquired at the National Center for CryoEM Access and Training (NCCAT) and at the Pacific Northwest Center for Cryo-EM using a Titan Krios microscope (Thermo-Fisher) operating at 300 kV and controlled by Leginon (NCCAT) or SerialEM (PNCC) software. Detailed information regarding the frames, dosages, magnifications, pixel sizes, and defocus values for each dataset is provided in *SI Appendix*, Table S1.

CryoEM Data Processing. CryoEM data were processed using cryoSPARC v4 (32). Following alignment of movie frames by Patch Motion Correction, contrast transfer function (CTF) parameters were estimated using Patch CTF Estimation (33). Extensive particle picking was performed to obtain particle stacks enriched for side-on, top-down, and even oblique views of pMMO or AMO embedded in membranes. Templates generated from a single particle cryoEM structure of pMMO in nanodiscs (EMD-24826) were used to guide initial template picking, and extensive 2D classification, heterogeneous refinement, and 3D classification were used to prune the particle stack and obtain a preliminary 3D reconstruction. The optimized particle stack was used to train a Topaz picking model (34, 35), which yielded a particle stack processed as above, this time with further homogeneous, nonuniform, and CTF refinements.

These extracted particles were used for 2D classification, from which good classes were selected to serve as templates for further refinement. Particles chosen using these templates were refined through heterogeneous refinement with C1 symmetry, using a previously published pMMO volume (EMD-24826) as a reference against the same volume lowpass filtered as a decoy reference.

This process was repeated with a box size of 128 pixels until the estimated resolution approached the Nyquist limit. The refined particles were then subjected to homogeneous refinement with C1 symmetry, nonuniform refinement at C1 symmetry, and nonuniform refinement at C3 symmetry, all with dynamic masking (36). Iterative global CTF refinements were then performed, alternating with masked nonuniform refinements at C3 symmetry to improve resolution and map quality. The resulting volume was considered final when the resolution stopped improving. Additionally, the effectiveness of DeepEMhancer postprocessing was assessed for enhancing reconstruction clarity (37), but its application did not yield significant improvements to specific features of interest. Finally, local resolution estimation and filtering techniques were applied to sharpen the final volume. Resolution values were reported based on gold-standard Fourier shell correlation with a cutoff of 0.143 (38).

Structure Building and Visualization. Initial structural models were built automatically using ModelAngelo (27), with manual addition and refinement of copper centers and lipid molecules. Examination and adjustment of copper ligands, copper centers, and membrane-associated molecules were performed manually in Coot [version 0.9.8.93 EL (ccp4)] (39). Further refinement of the models involved iterative rounds of real-space refinement using the Phenix (version 1.21-5207) cryoEM suite along with automatic addition of waters (40), followed by manual inspection and refinement within Coot. Fitting of refined models into the cryoEM maps, visualization of structures, resampling of maps to uniform grid spacing, and thresholding of maps based on their sigma (σ) values, as well as figure generation, were performed using ChimeraX-1.7.1 (41).

Data, Materials, and Software Availability. The models of pMMO from *M. capsulatus* (Bath) and from *M.* sp. Rockwell along with the model for AMO from *N. europaea* have been deposited in the Protein Data Bank and Electron Microscopy Data Bank with accession codes PDB 9CL2/EMD-45659 (washed membranes) (42, 43), PDB 9CL3/EMD-45660 (unwashed membranes) (44, 45), PDB 9CL4/EMD-45661 (crosslinked washed membranes) (46, 47), PDB 9CL1/EMD-45658 (0.02% DDM) (48, 49), PDB 9CL5/EMD-45662 (*M.* sp. Rockwell) (50, 51), and PDB 9CL6/EMD-45663 (*N. europaea* AMO) (52, 53). The corresponding cryoEM maps are available at the Electron Microscopy Data Bank (https://www.ebi.ac.uk/emdb/). All other data are available in the main text or supplementary materials.

ACKNOWLEDGMENTS. The work on *M. capsulatus* (Bath) pMMO was supported by NIH Grant R35GM118035 (A.C.R.), and the work on *M.* sp. Rockwell pMMO and AMO was supported by Department of Energy Grant DE-SC0016284 (A.C.R.). F.J.T. was supported by NIH Grants T32GM105538 and F31ES034283, and the Northwestern University Rappaport Award for Research Excellence. This work used resources of the Northwestern Structural Biology Facility and the Northwestern Keck Biophysics Facility, which are supported by the NCI CCSG P30 CA060553 Grant awarded to the Robert H. Lurie Comprehensive Cancer Center. Some of this work was performed at the National Center for CryoEM Access and Training (NCCAT) and the Simons Electron Microscopy Center located at the New York Structural Biology Center, supported by the NIH Common Fund Transformative High-Resolution Cryo-Electron Microscopy program (U24 GM129539) and by Grants from the Simons Foundation (SF349247) and NY State Assembly. A portion of this research was supported by NIH Grant U24GM129547 and performed at the PNCC at OHSU and accessed

through EMSL (grid.436923.9), a DOE Office of Science User Facility sponsored by the Office of Biological and Environmental Research. We thank Supapat Visanpattanasin and Patrick McLean for help with data analysis and sample preparation. We thank Professor Daniel Arp for a gift of *N. europaea* cell mass. We thank Professor Lisa Stein and Dr. Marina Lazic for providing fresh *N. europaea* cell mass and Professor Lisa Stein for helpful discussions. We thank Professor Mary Lidstrom for helpful discussions, facilitated by a Grant from the Carbon Technology Research Foundation.

1. U. Singh *et al.*, Technological avenues and market mechanisms to accelerate methane and nitrous oxide emissions reductions. *iScience* **25**, 105661 (2022).
2. E. G. Nisbet *et al.*, Atmospheric methane and nitrous oxide: Challenges along the path to Net Zero. *Philos. Trans. A Math. Phys. Eng. Sci.* **379**, 20200457 (2021).
3. D. J. Arp, L. Y. Stein, Metabolism of inorganic N compounds by ammonia-oxidizing bacteria. *Crit. Rev. Biochem. Mol. Biol.* **38**, 471–495 (2003).
4. L. Y. Stein, M. E. Lidstrom, Greenhouse gas mitigation requires caution. *Science* **384**, 1068–1069 (2024).
5. F. J. Tucci, A. C. Rosenzweig, Direct methane oxidation by copper- and iron-dependent methane monooxygenases. *Chem. Rev.* **124**, 1288–1320 (2024).
6. R. Khadka *et al.*, Evolutionary history of copper membrane monooxygenases. *Front. Microbiol.* **9**, 2493 (2018).
7. S. Wendeborn, The chemistry, biology, and modulation of ammonium nitrification in soil. *Angew. Chem., Int. Ed. Engl.* **59**, 2182–2202 (2020).
8. R. L. Lieberman, A. C. Rosenzweig, Crystal structure of a membrane-bound metalloenzyme that catalyses the biological oxidation of methane. *Nature* **434**, 177–182 (2005).
9. S. M. Smith *et al.*, Crystal structure and characterization of particulate methane monooxygenase from *Methylocystis* species strain M. *Biochemistry* **50**, 10231–10240 (2011).
10. S. Sirajuddin *et al.*, Effects of zinc on particulate methane monooxygenase activity and structure. *J. Biol. Chem.* **289**, 21782–21794 (2014).
11. S. Y. Ro *et al.*, From micelles to bicelles: Effect of the membrane on particulate methane monooxygenase activity. *J. Biol. Chem.* **293**, 10457–10465 (2018).
12. M. O. Ross *et al.*, Particulate methane monooxygenase contains only mononuclear copper centers. *Science* **364**, 566–570 (2019).
13. S. Y. Ro *et al.*, Native top-down mass spectrometry provides insights into the copper centers of membrane-bound methane monooxygenase. *Nat. Commun.* **10**, 2675 (2019).
14. R. J. Jodts *et al.*, Coordination of the copper centers in particulate methane monooxygenase: Comparison between methanotrophs and characterization of the Cu_c site by EPR and ENDOR spectroscopies. *J. Am. Chem. Soc.* **143**, 15358–15368 (2021).
15. C. W. Koo, A. C. Rosenzweig, Biochemistry of aerobic biological methane oxidation. *Chem. Soc. Rev.* **50**, 3424–3436 (2021).
16. C. W. Koo, F. J. Tucci, Y. He, A. C. Rosenzweig, Recovery of particulate methane monooxygenase activity in a lipid bilayer. *Science* **375**, 1287–1291 (2022).
17. F. J. Tucci, R. J. Jodts, B. M. Hoffman, A. C. Rosenzweig, Product analog binding identifies the copper active site of particulate methane monooxygenase. *Nat. Catal.* **6**, 1194–1204 (2023).
18. M. R. Hyman, P. M. Wood, Methane oxidation by *Nitrosomonas europaea*. *Biochem J* **212**, 31–37 (1983).
19. D. J. Arp, L. A. Sayavedra-Soto, N. G. Hommes, Molecular biology and biochemistry of ammonia oxidation by *Nitrosomonas europaea*. *Arch. Microbiol.* **178**, 250–255 (2002).
20. S. A. Ensign, M. R. Hyman, D. J. Arp, In vitro activation of ammonia monooxygenase from *Nitrosomas europaea* by copper. *J. Bacteriol.* **175**, 1971–1980 (1993).
21. A. B. Hooper, K. R. Terry, Specific inhibitors of ammonia oxidation in *Nitrosomonas*. *J. Bacteriol.* **115**, 480–485 (1973).
22. B. Krishnarjuna, A. Ramamoorthy, Detergent-free isolation of membrane proteins and strategies to study them in a near-native membrane environment. *Biomolecules* **12**, 1076 (2022).
23. Y. A. Zhu *et al.*, Structure and activity of particulate methane monooxygenase arrays in methanotrophs. *Nat. Commun.* **13**, 5221 (2022).
24. A. Kitmitto, N. Myronova, P. Basu, H. Dalton, Characterization and structural analysis of an active particulate methane monooxygenase trimer from *Methylococcus capsulatus* (Bath). *Biochemistry* **44**, 10954–10965 (2005).
25. E. A. Hoffman, B. L. Frey, L. M. Smith, D. T. Auble, Formaldehyde crosslinking: A tool for the study of chromatin complexes. *J. Biol. Chem.* **290**, 26404–26411 (2015).
26. S. L. Davies, R. Whittenbury, Fine structure of methane and other hydrocarbon-utilizing bacteria. *J. Gen. Microbiol.* **61**, 227–232 (1970).
27. K. Jamali *et al.*, Automated model building and protein identification in cryo-EM maps. *Nature* **628**, 450–457 (2024).
28. E. F. Liew, D. C. Tong, N. V. Coleman, A. J. Holmes, Mutagenesis of the hydrocarbon monooxygenase indicates a metal centre in subunit-C, and not subunit-B, is essential for copper-containing membrane monooxygenase activity. *Microbiology* **160**, 1267–1277 (2014).
29. W.-H. Chang *et al.*, Copper centers in the cryo-EM Structure of particulate methane monooxygenase reveal the catalytic machinery of methane oxidation. *J. Am. Chem. Soc.* **143**, 9922–9932 (2021).
30. R. G. Murray, S. W. Watson, Structure of *Nitrosocystis oceanus* and comparison with *Nitrosomonas* and *Nitrobacter*. *J. Bacteriol.* **89**, 1594–1609 (1965).
31. S. Sirajuddin, A. C. Rosenzweig, Enzymatic oxidation of methane. *Biochemistry* **54**, 2283–2294 (2015).
32. A. Punjani, J. L. Rubinstein, D. J. Fleet, M. A. Brubaker, cryoSPARC: Algorithms for rapid unsupervised cryo-EM structure determination. *Nat. Methods* **14**, 290–296 (2017).
33. K. Zhang, Gctf: Real-time CTF determination and correction. *J. Struct. Biol.* **193**, 1–12 (2016).
34. T. Bepler *et al.*, Positive-unlabeled convolutional neural networks for particle picking in cryo-electron micrographs. *Nat. Methods* **16**, 1153–1160 (2019).
35. T. Bepler, K. Kelley, A. J. Noble, B. Berger, Topaz-denoise: General deep denoising models for cryoEM and cryoET. *Nat. Commun.* **11**, 5208 (2020).
36. A. Punjani, H. Zhang, D. J. Fleet, Non-uniform refinement: Adaptive regularization improves single-particle cryo-EM reconstruction. *Nat. Methods* **17**, 1214–1221 (2020).
37. R. Sanchez-Garcia *et al.*, DeepEMhancer: A deep learning solution for cryo-EM volume post-processing. *Commun. Biol.* **4**, 874 (2021).
38. S. H. Scheres, S. Chen, Prevention of overfitting in cryo-EM structure determination. *Nat. Methods* **9**, 853–854 (2012).
39. P. Emsley, K. Cowtan, Coot: Model-building tools for molecular graphics. *Acta Cryst.* **D60**, 2126–2132 (2004).
40. P. D. Adams *et al.*, PHENIX: A comprehensive python-based system for macromolecular structure solution. *Acta Cryst.* **D66**, 213–221 (2010).
41. E. F. Pettersen *et al.*, UCSF ChimeraX: Structure visualization for researchers, educators, and developers. Protein Sci. 30, 70–82 (2021).
42. F. J. Tucci, A. C. Rosenzweig, Particulate methane monooxygenase in washed native membranes. Protein Data Bank. https://www.rcsb.org/structure/9CL2. Deposited 8 July 2024.
43. F. J. Tucci, A. C. Rosenzweig, Particulate methane monooxygenase in washed native membranes. Electron Microscopy Data Bank. https://www.ebi.ac.uk/emdb/EMD-45659. Deposited 8 July 2024.
44. F. J. Tucci, A. C. Rosenzweig, Particulate methane monooxygenase in unwashed native membranes. Protein Data Bank. https://www.rcsb.org/structure/9CL3. Deposited 8 July 2024.
45. F. J. Tucci, A. C. Rosenzweig, Particulate methane monooxygenase in unwashed native membranes. Electron Microscopy Data Bank. https://www.ebi.ac.uk/emdb/EMD-45660. Deposited 8 July 2024.
46. F. J. Tucci, A. C. Rosenzweig, Particulate methane monooxygenase in crosslinked, washed native membranes. Protein Data Bank. https://www.rcsb.org/structure/9CL4. Deposited 8 July 2024.
47. F. J. Tucci, A. C. Rosenzweig, Particulate methane monooxygenase in crosslinked, washed native membranes. Electron Microscopy Data Bank. https://www.ebi.ac.uk/emdb/EMD-45661. Deposited 8 July 2024.
48. F. J. Tucci, A. C. Rosenzweig, Particulate methane monooxygenase in 0.02% DDM. Protein Data Bank. https://www.rcsb.org/structure/9CL1. Deposited 8 July 2024.
49. F. J. Tucci, A. C. Rosenzweig, Particulate methane monooxygenase in 0.02% DDM. Electron Microscopy Data Bank. https://www.ebi.ac.uk/emdb/EMD-45658. Deposited 8 July 2024.
50. F. J. Tucci, A. C. Rosenzweig, Particulate methane monooxygenase in native membranes. Protein Data Bank. https://www.rcsb.org/structure/9CL5. Deposited 8 July 2024.
51. F. J. Tucci, A. C. Rosenzweig, Particulate methane monooxygenase in native membranes. Electron Microscopy Data Bank. https://www.ebi.ac.uk/emdb/EMD-45662. Deposited 8 July 2024.
52. F. J. Tucci, A. C. Rosenzweig, Ammonia monooxygenase in native membranes. Protein Data Bank. https://www.rcsb.org/structure/9CL6. Deposited 8 July 2024.
53. F. J. Tucci, A. C. Rosenzweig, Ammonia monooxygenase in native membranes. Electron Microscopy Data Bank. https://www.ebi.ac.uk/emdb/EMD-45663. Deposited 8 July 2024.